Icing Physics Studies Using the 3D SIDRM Test Article: Aerodynamic and Supercooled Liquid Icing Analysis

Tadas P. Bartkus
Ohio Aerospace Institute, Cleveland, OH, 44142, USA

Sam Lee
HX5, LLC, Cleveland, OH, 44135, USA

Eric A. Stewart
Naval Air Warfare Center Aircraft Division, Patuxent River, MD, 20670, USA

Abstract

In-flight icing is an important safety issue and is a factor that affects aircraft design and performance. Newer regulations are driving a need for improvements in airframe and engine icing simulation capability. Experimental data is required for development of icing physics models and simulation validation. To that end, this paper presents the analysis of the supercooled liquid icing data subset from tests conducted in 2022 at the NASA Icing Research Tunnel that studied both supercooled water and ice-crystal icing. The test article that was utilized replicated 3D geometrical features of an inter-compressor duct and strut region of a turbofan engine. The surfaces of the Simulated Inter-compressor Duct Research Model (SIDRM) can be heated to simulate the warm surfaces of the turbofan inter-compressor duct. The test article is instrumented with pressure taps, heaters, heat flux gauges, and thermocouples, while a 3D laser scanner, cameras, and a scale to measure ice mass were utilized to characterize the icing behavior. The aim of these tests was to generate ice accretions on the SIDRM test article under well-characterized supercooled liquid icing and ice crystal icing conditions. This paper discusses measurements related to aerodynamic testing and supercooled liquid icing tests that were conducted. Aerodynamic measurements were analyzed and compared to computational simulations and were found to be in good agreement for the range of airspeeds (50 to 230 knots) and angles of attack (0 to 4°) tested. Various parametric sweeps were conducted during the supercooled liquid icing portion of the test entry (cloud median volumetric diameter ranged from 15 to 90 µm, total air temperature from -3 to -17 °C, angle of attack from 0 to 4°, and accretion time from 5 to 20 min). These sweeps were performed to measure that parameter's impact on ice accretion size, location (icing extent), characteristics (such as glaze/rime ice and shedding behavior), and test article surface temperature. Analysis of the test data showed that clouds composed of larger drops, colder air temperatures, smaller angles of attack, and longer spray times were the primary parameters that resulted in accretions with greater ice mass. Test article angle of attack and cloud droplet size influenced the location of ice accretion as these two parameters directly impact collection efficiency. With respect to icing characteristics, total air temperature dictated icing type, and smaller cloud drop size along with warmer air temperatures resulted in greater amounts of ice shedding. Surface temperature increased during ice accretion from the release of latent (fusion) heat, where total air temperature and cloud drop size impacted the amount of surface temperature change. The icing measurements collected during the SIDRM tests will be used to develop and validate 3D computational engine icing tools, such as GlennICE, that predictively assesses the onset and growth of ice. One of the goals of the sponsoring NASA project is to develop simulation models and tools that can assist in the design and certification of engines for flight in icing conditions in a cost-effective way.

Introduction

Numerous reports of turbofan engine power-loss or damage events have been attributed to the ingestion of ice crystals [1]. These events typically occur in deep convective updraft systems and have included engine stall, rollback, flameout, surge, and engine component damage. Mason et al. [2] hypothesized that ice crystals ingested into the engine undergo partial melting within the warm compressor system and then, as a mixed-phase water mass, accrete on surfaces within the engine core. Research efforts in understanding the physics of ice crystal icing have grown to address this threat of engine icing. The National Aeronautics and Space Administration (NASA) Glenn Research Center has been conducting experiments to better understand ice crystal icing. Multiple engine tests have been conducted at the NASA Propulsion Systems Laboratory (PSL) icing wind tunnel since the tunnel's spray bar installation [3-5]. In addition, experimental studies on the fundamental physics of ice crystal icing have been conducted at the NASA PSL tunnel [6-9].

The first two test entries in this series of fundamental ice crystal icing research tests were conducted in the NASA PSL tunnel in 2016 [8] and 2018 [6, 7]. The aim of these tests was to generate ice accretions on a NACA0012 airfoil under well-characterized conditions [6, 7]. Ice shapes were generated across different flow conditions. The 2016 experimental calibration efforts were limited to centerline measurements. An instrument traversing system was developed for the 2018 tests which allowed for the ability to perform flow surveys at various positions within the cloud at the tunnel exit plane. Ice geometry measurements were limited to extracting 1D and 2D ice shapes from orthogonal video images that captured the ice growth at the NACA0012 leading edge.

Most recently NASA conducted the next test series of fundamental icing physics tests at the NASA Icing Research Tunnel (IRT) [10-11]. These icing wind tunnel tests were conducted in early 2022. These tests utilized the Simulated Inter-compressor Duct Research Model

(SIDRM), a 3D test article whose geometry is representative of an inter-compressor duct and strut region of a turbofan engine. The test article has the ability to heat its surfaces to simulate the warm surfaces of the turbofan inter compressor duct, and is instrumented with heaters, heat flux gauges, thermocouples, and pressure taps. These tests, however, did not fully simulate the environment within the engine. The testing air temperatures were below freezing, and the icing clouds were fully glaciated before making impact with the test article surface. It is believed that ingested ice crystal clouds are partially melted as they pass through warm engine passages before impacting internal engine components. In addition, this open geometry will result in different pressures and flow compared to the ducted region of the compressor.

The aim of these tests was to generate ice accretions on the SIDRM test article under well-characterized conditions. Icing tests were conducted under ice crystal icing and supercooled water icing conditions. This paper focuses on the analysis of the supercooled liquid icing data subset. Supercooled liquid icing tests provide simulation validation data on a 3D geometry, in addition an estimate of collection efficiency can be back-calculated from ice accretion geometry which is also required for ice crystal icing simulation. The IRT is well calibrated for supercooled water icing, but not for ice crystal icing clouds. To that end, ice crystal cloud characterization tests were conducted to provide proper conditions for ice crystal icing tests. The icing physics data measured during these tests will be used to develop and validate 3D engine icing simulation tools such as GlennICE [12-14]. The intent is to provide analyzed results related to ice crystal icing in a future technical paper.

This paper provides analysis results and discussions from the supercooled liquid icing and the test article aerodynamic characterization portions of the test entry. This paper, along with an accompanying conference paper by Stewart et al. [15] build upon the work by Bartkus et al. [10]. These testing efforts are part of NASA's Advanced Air Transport Technology (AATT) Project activities to improve understanding of the ice growth physics and advance engine aero thermodynamic modeling tools to predictively assess the onset and growth of ice in current and future engines during flight. Simulation tools like GlennICE will allow industry to design and certify engines for flight in icing conditions in a cost-effective way.

Experimental Data Analysis and Discussion

A limited description of the experimental set-up is provided here. For the interested reader, a more detailed description is provided by Bartkus et al. [10] elsewhere. These tests utilized the SIDRM test article, which is shown in Fig. 1. SIDRM aerodynamic analysis and supercooled liquid icing analysis along with discussion are provided in the following two subsections.

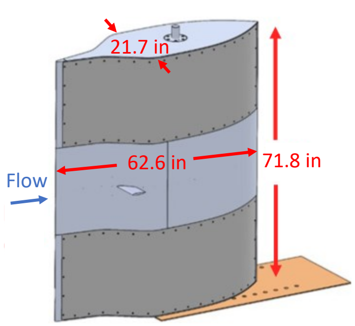

Figure 1. SIDRM test article schematic and dimensions with floor mounting plate at the bottom.

SIDRM Aerodynamic Analysis

Test article aerodynamic analysis was performed utilizing pressure tap measurements. The test article contains 64 pressure taps in total, split between two rows on the upper and lower portions that run the chord length of the test article. Figures 2 and 3 are schematics showing the location of the upper and lower pressure tap rows (labeled as P###). These images also show the *x*, *y*, *z*, coordinate system. Figure 2 also shows the location of Type-K thermocouples that are flush-mounted on the outer surface (labeled as T### and ST#). The side that can be seen in Fig. 2 is considered the "instrumented" side as it contains the majority of the thermocouple and heat flux gauge instrumentation. The other side of the test article (not visible in the Fig. 2) contains limited instrumentation, largely for monitoring purposes, and will be referred to the "non-instrumented" side in this paper. Tables A1 and A2 in the appendix provide surface locations of the Type-K thermocouples and pressure taps respectively.

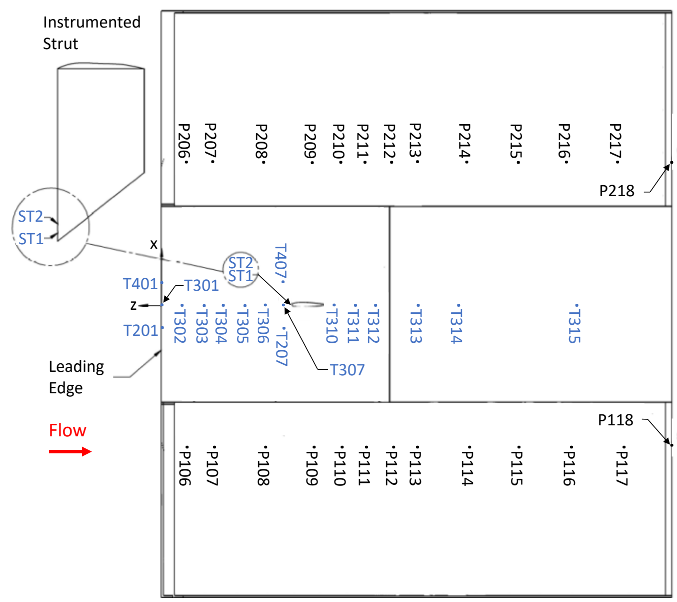

Figure 2. Schematic of pressure tap and thermocouple locations on SIDRM. The opposite side (non-instrumented side) is not shown but the pressure tap locations mirror the side that is shown (instrumented side).

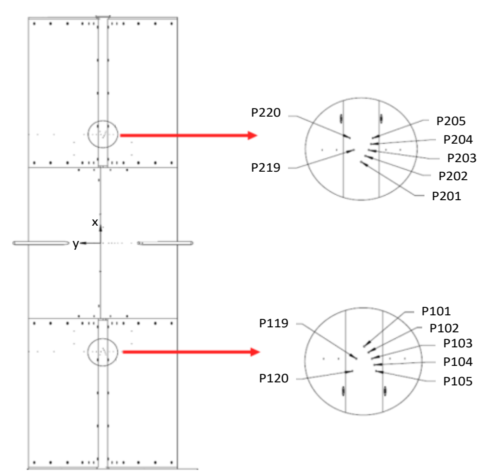

Figure 3. Schematic of pressure tap locations on SIDRM staggered at the leading edge. Flow direction is into the paper.

Aerodynamic characterization was performed varying test article angles of attack (*AoA* = 0, 1, 2, 3, and 4°) and airspeed (*U* = 50, 100, 150, 200, and 230 knots). Table 1 shows the aerodynamic conditions that were run. The pressure coefficient, C_p, was calculated from experimental measurements. Equation 1 shows the pressure coefficient expression where P_{tap} is the surface pressure as measured by the tap, P_s is the freestream static pressure, and P_0 is the total pressure. Total and static pressure measurements were made by the North and South pitot-static probes located at the entrance of the IRT test section.

Table 1. Tabulation of aerodynamic test conditions that were conducted.

AoA (°)	0	0	0	0	0	1	2	3	4	4	4	4	4
U (knots)	50	100	150	200	230	150	150	150	50	100	150	200	230

$$C_p = \frac{P_{tap} - P_s}{P_0 - P_s} \quad (1)$$

Two-dimensional (2D) computational fluid dynamics (CFD) simulations were performed to compare with experimental aerodynamic pressure measurements. With the struts located far from the pressure taps and not impacting pressure measurements, performing 2D simulations was sufficient for comparison with pressure measurements. SIDRM's main body (no struts) was meshed inside the IRT's tunnel geometry using a 2D mesh that was 1-cell deep at a total cell count near 60,000. SIDRM's high flow blockage causes the preference of a rectangular tunnel grid over a circular far-field grid. The inlet and outlet of the IRT was extended out about 12 chord lengths from the test article. Angle of attack changes were created by rotating the test article within the IRT geometry and creating a new mesh. The mesh was composed of using a hybrid mesh of prism layers (with y+ ~1) at the surface and unstructured tetrahedral in the rest of the volume grid. Refinement was placed around the test article and downstream to capture the wake. CFD simulations were run in ANSYS Fluent using the k-Omega SST turbulence model with viscous heating and curvature correction enabled. Velocity inlet and pressure outlet boundary conditions were applied, with a no-slip surface condition on the test article. The tunnel walls were simulated with an inviscid boundary condition. Static pressures and total temperatures were kept the same for all angle of attack runs. SIDRM's separation near the trailing edge required running thousands of iterations until the coefficients of lift and drag plateaued reaching steady-state convergence.

Figure 4 shows that there is good agreement between CFD predictions (black solid curve) and experimental measurements (curves with symbols) for a test run where airspeed was 150 knots, and the test article was at a 0° angle of attack. The pressure coefficients are plotted against the normalized chord length (*z* represents the chord direction, *c* is the chord length). The pressure tap measurements are plotted as four separate sections of the model to visualize any variation between sides. The upper and lower pressure tap rows are split between the two sides of the model (instrumented and non-instrumented sides). At 0° AoA, all four experimental measurements are expected to collapse on top of each other as flow is symmetric and no variation is expected between the upper and lower rows. The simulation predicted flow separation beyond *z/c* = -0.8 where the *Cp* flattens to the trailing edge and is in close agreement with experiment. Separation beyond *z/c* = -0.8 was also visually observed when utilizing tufts as shown in Fig. 5.

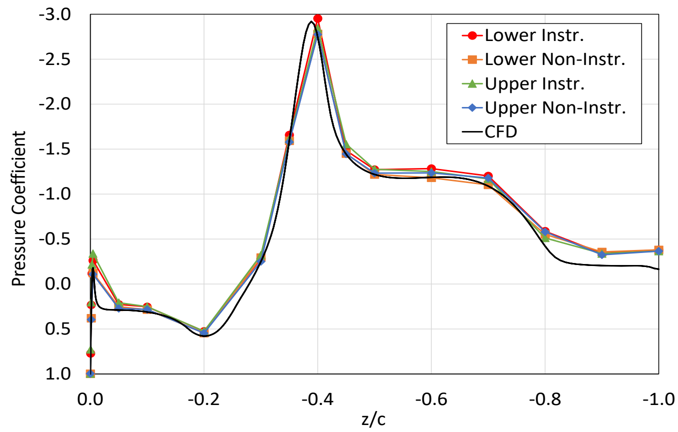

Figure 4. Pressure coefficient plotted against normalized chord-length for a test run at 150 knots and 0° AoA. Experimental values are depicted in lines with symbols, while the CFD prediction is shown as a solid line. Note that the bottom axis values are negative because of the coordinate convention used.

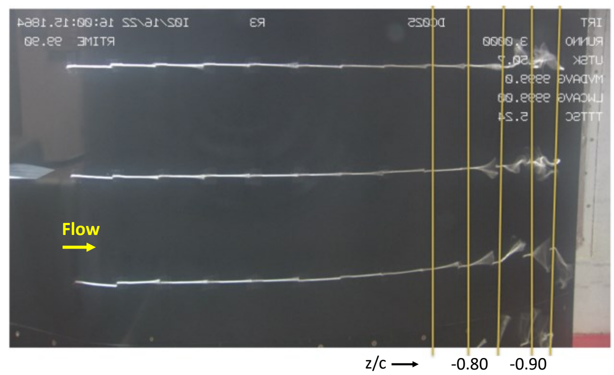

Figure 5. Image of tufts on the back half of the test article showing where flow became detached. Flow is left to right.

Figure 6 shows measured pressure coefficients plotted against normalized chord-length for various airspeeds at 4° AoA, which is in good agreement with CFD predictions shown in Fig. 7. There is generally good agreement between experiment and CFD regarding the C_p spike on the suction side near the leading edge for these 4° AoA tests. The continuously decreasing value of C_p (more negative) at *z/c* = -0.4 with increasing velocity is due to Reynolds number effect (Re = 1 x 10^6 to 5 x 10^6) [16]. Greater momentum from faster airspeeds pushes the location of separation farther downstream, which in turn aids airspeed and affects C_p upstream at the model's thickest width. The pressure taps are too coarsely distanced to capture the exact location of most negative C_p around *z/c* = -0.4 as can be seen in the CFD predictions. Also, of note here is that at an angle of attack (in this case 4° AoA), the lift generated at the front half of the test article is countered by negative lift on the aft half. In the forward half, the upper curves represent the suction side, the lower curves represent the pressure side. Integrating the difference between the two provides the amount of lift generated by the forward half. In the aft half, the upper curves represent the pressure side, the lower curves the suction side. The integrated difference now produces negative lift (a downward force) on the aft half. While the SIDRM geometry produces lift poorly at non-zero angles of attack, the intent for varying AoA is to investigate its impact on local collection efficiency, including shadow and concentration regions during icing tests.

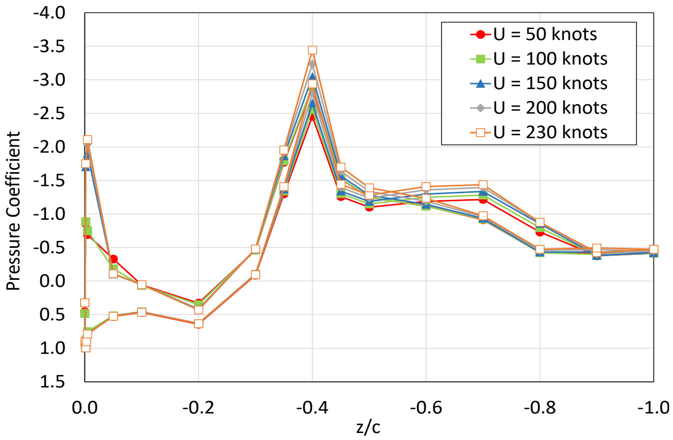

Figure 6. Measured pressure coefficients plotted against normalized chord-length for various airspeeds at 4° AoA.

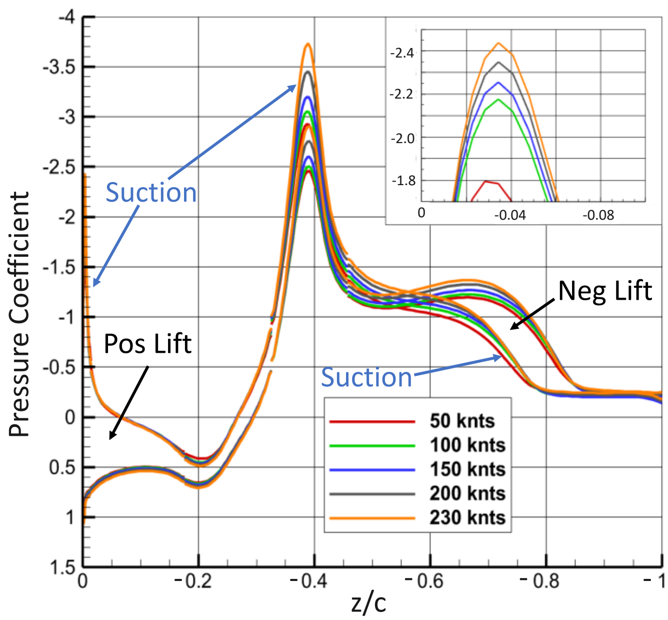

Figure 7. CFD predictions of pressure coefficients plotted against normalized chord-length for various airspeeds at 4° AoA. The inset in the CFD simulation provides a zoomed in view of the suction side spike near the leading edge.

Figure 8 shows a zoomed in view of pressure coefficient measurements near the SIDRM leading edge at various angles of attack at 150 knots. The pressure coefficients are plotted against surface wrap distance, *s*, where the test article's geometric leading edge is at 0 inches at 0° AoA. The red curve represents 0° AoA and is not symmetric around 0 inches (if the stagnation line is at 0, then *Cp* symmetry is expected). The plotted curves suggest that the stagnation point is between 0 and 1° AoA. This could mean there is a small flow angularity, the model itself is not perfectly symmetrical, the turntable is not perfectly at 0° AoA (even though measurement says it is 0°), or some combination of these factors. This is to say that when SIDRM is set to 0° AoA, it may more accurately be about 0.3° AoA, for example (rotated such that the instrumented side is the slight suction side). Future tests will investigate this observed slight asymmetric flow more closely.

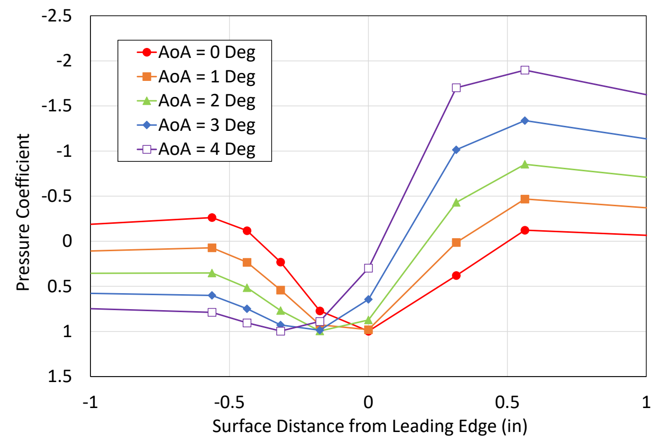

Figure 8. Pressure coefficient measurements against surface distance near the SIDRM leading edge at various angle of attacks at 150 knots.

Supercooled Liquid Icing Analysis

Twenty-eight (28) supercooled liquid icing test runs were conducted during the test entry and are discussed here. Various parameter sweeps were performed to measure that parameter's impact on ice accretion size, location, characteristics (such as glaze/rime ice and shedding behavior), and test article surface temperature, and is organized in this section accordingly. Primary parameter variation sweeps included cloud median volumetric diameter (*MVD*), total air temperature (T_0), angle of attack, and accretion time.

Table 2 shows the target test conditions at the test section and is ordered in blocks according to the 7 parameter sweeps (Blocks A – G). Three MVD sweeps (Blocks A – C) were conducted at varying airspeeds, angles of attack, and accretion times. A total air temperature sweep was conducted that ranged from glaze to rime ice (Block D). An angle of attack sweep (Block E) was performed along with two accretion time sweeps for rime ice (Block F) and glaze ice (Block G) conditions. Positive angle of attack values mean that the test article was rotated in the direction that made the instrumented side the pressure side. Unique test runs are identified by their test ID (UG####). In the table, liquid water content is noted as *LWC*. The static relative humidity is approximated to be saturated at the test section for this atmospheric icing wind tunnel as an equilibration spray was performed at the start of each day of testing. Five test points were repeated to provide a measure of repeatability (e.g., UG3540 and UG3547 in Block B). Five test runs are duplicated in different parameter sweeps in this table (e.g., UG3540 in Blocks B and E).

Table 2. Tabulation of test conditions and ice accretion measurements for three MVD sweeps, a total air temperature sweep, and angle of attack sweep, and two accretion time sweeps for rime and glaze ice conditions. Values denoted by asterisks refer to test runs where measurement of ice mass on the struts were affected by ice sheds.

	Target Test Conditions						Ice Accretion Measurements		
Col 1	Col 2	Col 3	Col 4	Col 5	Col 6	Col 7	Col 8	Col 9	Col 10
Test ID (#)	Accretion Time (min)	T_0 (°C)	U (knots)	AoA (°)	MVD (μm)	LWC (g/m^3)	Both Struts Ice Mass (g)	Main Body Ice Mass (g)	LE Ice Vol. (cm^3)
Block A: MVD Sweep at 150 knots, 0° AoA, and 10 min accretion time									
UG3513	10	-17	150	0	15	0.45	66	172	56.3
UG3514	10	-17	150	0	18	0.45	70	221	62.3
UG3518	10	-17	150	0	30	0.45	79	407	78.8
UG3515	10	-17	150	0	50	0.45	79	548	87.1
UG3516	10	-17	150	0	90	0.45	83	781	93.7
Block B: MVD Sweep at 150 knots, 4° AoA, and 5 min accretion time									
UG3541	5	-17	150	4	18	0.45	33	105	35.5
UG3540	5	-17	150	4	30	0.45	35	176	40.0
UG3547	5	-17	150	4	30	0.45	33	184	39.4
UG3537	5	-17	150	4	50	0.45	34	N/A	41.1
UG3546	5	-17	150	4	50	0.45	33	249	42.6
UG3542	5	-17	150	4	90	0.45	36	382	44.9
Block C: MVD Sweep at 200 knots									
UG3520	7	-17	200	0	18	0.45	59	239	59.4
UG3521	7	-17	200	0	30	0.45	63	376	68.1
UG3548	7	-17	200	0	30	0.45	64	377	72.8
UG3535	7	-17	200	0	50	0.45	65	574	84.4
UG3536	7	-17	200	0	90	0.45	64	772	86.4
Block D: T_0 Sweep									
UG3531	20	-3	150	4	25	0.50	139*	395	147.8
UG3545	20	-3	150	4	25	0.50	132*	393	147.9
UG3530	20	-6	150	4	25	0.50	247	477	136.6
UG3544	20	-6	150	4	25	0.50	234	480	137.5
UG3532	20	-9	150	4	25	0.50	239	526	156.6
UG3533	20	-12	150	4	25	0.50	238	551	170.0
UG3534	20	-17	150	4	25	0.50	224	595	172.6
Block E: AoA Sweep									
UG3538	5	-17	150	0	30	0.45	33	208	43.9
UG3539	5	-17	150	2	30	0.45	33	205	42.7
UG3543	5	-17	150	3	30	0.45	35	188	39.8
UG3540	5	-17	150	4	30	0.45	35	176	40.0
UG3547	5	-17	150	4	30	0.45	33	184	39.4
Block F: Accretion Time Sweep (Rime Ice)									
UG3541	5	-17	150	4	18	0.45	33	105	35.5
UG3519	10	-17	150	4	18	0.45	73	208	66.5
Block G: Accretion Time Sweep (Glaze Ice)									
UG3549	10	-3	150	4	25	0.50	85	221	65.0
UG3531	20	-3	150	4	25	0.50	139*	395	147.8
UG3545	20	-3	150	4	25	0.50	132*	393	147.9

The primary measurements to assess ice accretion size for these tests were 3D laser scans of the final ice accretion and weighing of the accreted ice. The accreted ice geometry was measured after each test run utilizing a 3D laser scanner. Hexagon's Romer Absolute SI 7530 scanner was used and has a repeatability accuracy of +/- 0.003". The center 10-in (0.25-m) span was scanned from the leading edge to the extent of ice on either side of the test article, including the struts. Figure 9 depicts the area that was scanned with resulting 3D image of the ice accretion in the upper right of the figure. After scanning, the center 8-in (0.20-m) span of accreted ice was carefully cut from the leading edge to the extent of icing on both sides, removed, and weighed. Ice accreted on the struts was weighed separately. The combined ice mass from both struts is provided in Column 8 of Table 2. The ice mass as measured from the 8-in wide strip on the main body is provided in Column 9 of Table 2. It should be noted that the accreted ice on the suction side strut had shed towards the end of the icing test for Test ID# UG3531 and UG3545 of the total air temperature sweep, thus resulting in low strut ice mass measurements. From the 3D laser scans, the volume around the leading edge (LE) was calculated to provide an estimate of how various parameter sweeps impacted ice accretion. A clean 3D scan of the SIDRM test article was subtracted from the 3D scans of the accreted ice. The center 8-in span of the 3D scan was used in the volume calculation, with a cut in the *xy*-plane at z = -0.5 inches deep into the model leading edge. The volume of ice is shown in the bottom right of Fig. 9 and is quantified in the Column 10 of Table 2.

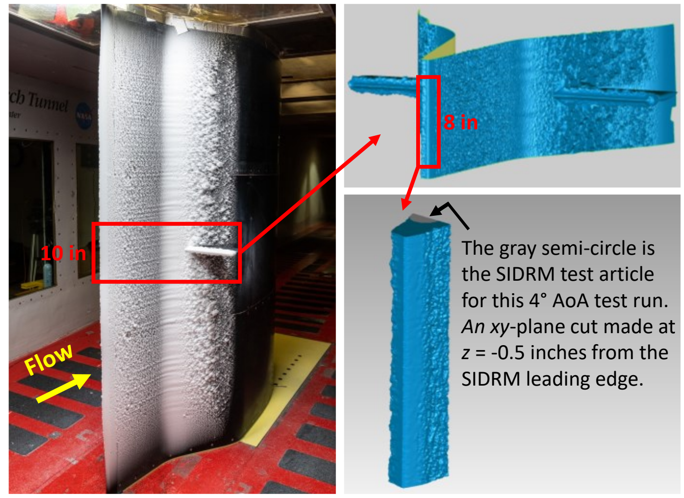

Figure 9. Ice accreted on the SIDRM test article on the left (Test Run ID UG3534), with the 10-in wide scanned region shown in the upper right, and the 8-in span length used to calculate the accreted ice volume at the leading edge shown in the bottom right.

Ice Accretion Size

Multiple parameters impacted accretion size. According to the main body ice mass measurements (Column 9 in Table 2), larger cloud MVD, colder air temperatures, smaller angles of attack, and longer spray times were the primary parameters that resulted in greater ice mass. This trend is consistent even when the ice masses from the struts and the main body are combined. In all 3 MVD sweeps, larger MVD clouds resulted in greater ice mass. Larger drops behave more ballistically while smaller drops follow the air flow more closely. In turn, the larger drops resulted in greater collection efficiency which directly impacts accreted ice mass. For the conditions tested in the total air temperature sweep, colder air temperatures resulted in greater ice mass measurements. Greater amounts of shedding occurred in the inclined area where the strut is located during the warmer total air temperature test runs. The greater shedding amounts may be a result of weaker ice cohesion strength compared to colder accretions and feather accretions experiencing more drag due to accretion shape and size. This shedding difference accounts, in part, for the difference in final measured ice mass. Additional testing is required to determine if other mechanisms are contributing to ice mass differences. For the conditions tested in the angle of attack sweep, increased angles of attack resulted in smaller ice mass. An increase in angle of attack resulted in more shadow regions where the cloud did not impact the test article surface, reducing ice accretion mass. Finally, a longer spray time resulted in greater ice mass. For both the glaze and rime condition accretion time sweeps, doubling spray time resulted in nearly twice the accreted ice mass on the main body (slightly less than double for the glaze condition test run).

Figures 10 through 16 show cross section cuts at the test article midspan for the corresponding 7 sweeps tabulated in Table 2. These figures provide an overall picture of where the ice accreted on the test article. Insets are provided to show greater ice accretion detail at the leading edge and both junctions where the struts meet the main body.

The ice accretion size trends in these figures are in agreement with the main body ice mass measurement trends from Table 2. These 7 figures show that larger ice cross sections resulted when tests were conducted with larger MVD clouds, colder air temperatures, smaller test article angle of attack, and longer accretion times. Flow is from top to bottom in Figs. 10 – 16. For test runs conducted at a non-zero angle of attack, the left side of the test article experienced pressure forces and the right side experienced suction forces in Figs. 10 – 16.

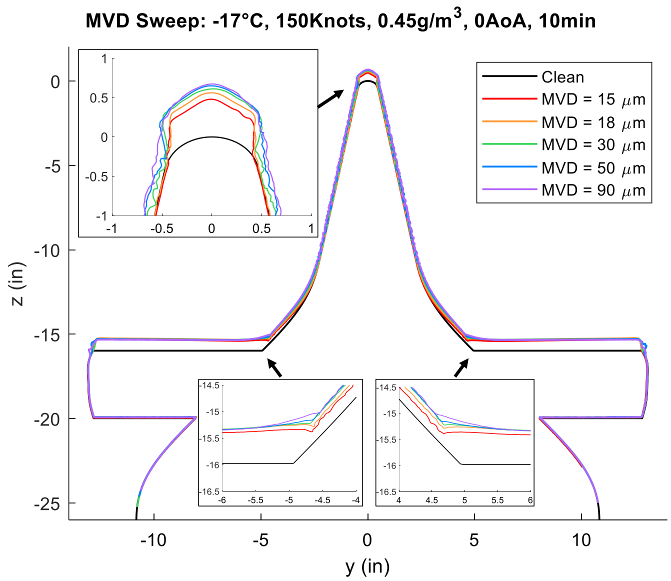

Figure 10. Cross sections at the midspan of the SIDRM test article for the MVD parameter sweep at 150 knots, 0° AoA, and 10 min accretion time (Block A).

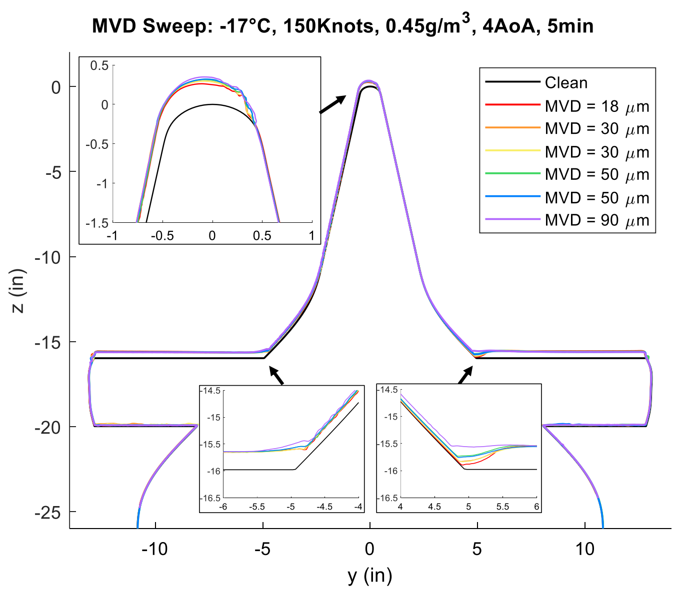

Figure 11. Cross sections at the midspan of the SIDRM test article for the MVD parameter sweep at 150 knots, 4° AoA and 5 min accretion time (Block B).

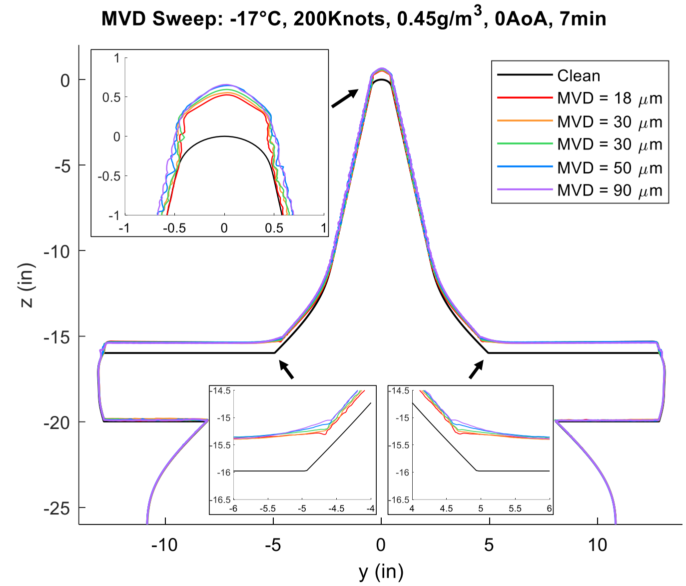

Figure 12. Cross sections at the midspan of the SIDRM test article for the MVD parameter sweep at 200 knots (Block C).

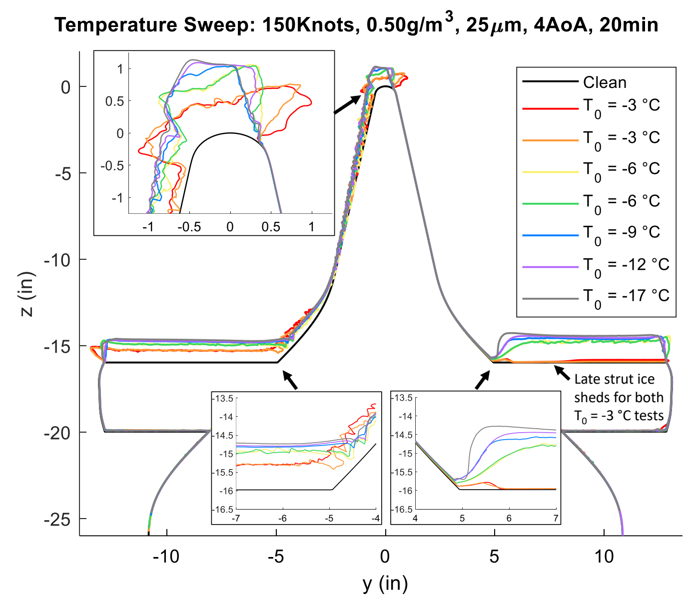

Figure 13. Cross sections at the midspan of the SIDRM test article for the air temperature parameter sweep (Block D). Note that the ice shed from the right strut late in the test for both test runs at T_0 = -3 °C.

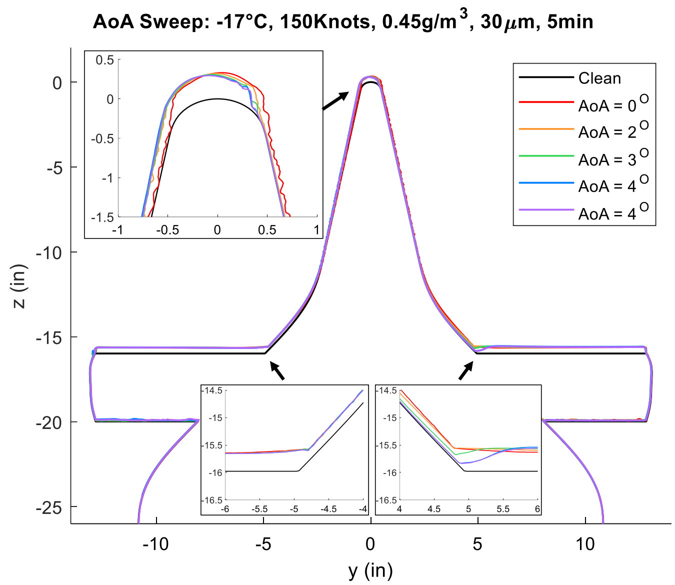

Figure 14. Cross sections at the midspan of the SIDRM test article for the angle of attack sweep (Block E).

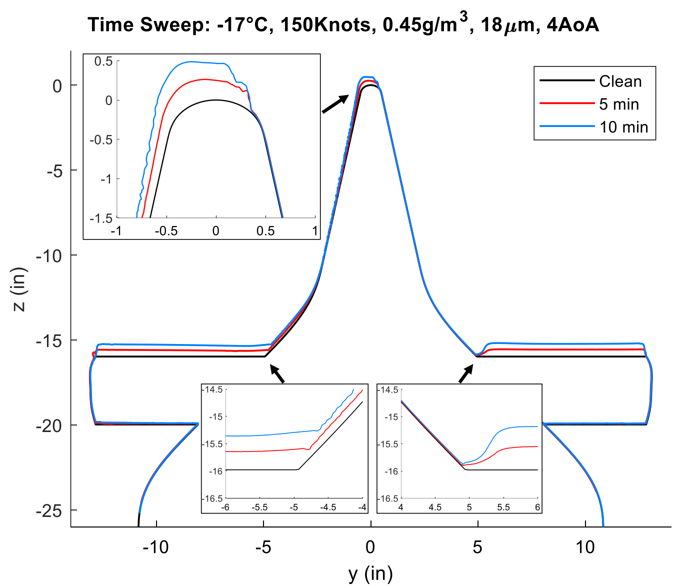

Figure 15. Cross sections at the midspan of the SIDRM test article for the accretion time sweep at rime ice conditions (Block F).

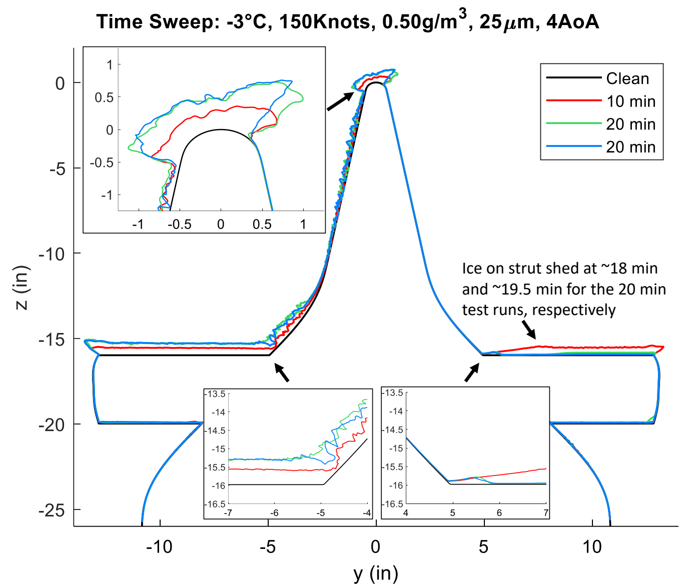

Figure 16. Cross sections at the midspan of the SIDRM test article for the accretion time sweep at glaze ice conditions (Block G).

The trend that greater ice mass accretions occurred with larger MVD clouds, colder air temperatures, smaller test article angle of attack, and longer accretion times is consistent with the leading edge volume calculations in Table 2, except for the total air temperature sweep. The volume trend in not monotonic with total air temperature. The LE volume measured at T_0 = -3 °C was greater than at T_0 = -6 °C, but as temperature continued to decrease transitioning towards rime ice, the measured LE volume increased. Figure 13 provides a visual of the changing LE ice accretion with decreasing temperature. Despite glaze ice accretion impacting LE volume such that it is not monotonic with decreasing total air temperature, the overall mass on the entire test article consistently increased monotonically with decreasing total air temperature.

There were 5 pairs of repeated test runs. Comparing the mass and volume measurements in Table 2, there was good repeatability between identical test runs. The average variation between identical test runs for strut ice mass, main body ice mass, and leading edge volume was 4%, 2%, and 3% respectively. Figures 11 through 13 (Blocks B, C, and D) contain these 5 repeated cases and provide a visual of the repeatability in ice accretion. This repeatability provides a good baseline and confidence in trends that are observed within individual parameter sweeps.

Ice Accretion Location

Figures 10 through 16 provide a visual reference for where icing generally occurred, indicating regions of greater collection efficiency. For any individual test run, greater amounts of ice accreted at the main body leading edge, the struts leading edges, and just upstream of the struts on the curved ramp section on the main body. Lower amounts of ice accretion occurred on the flat stretches aft of the main body leading edge (from z = -1 to 11 inches) and aft of the struts.

The most prominent parameters that impacted the location of ice accretion were angle of attack and cloud MVD. Test article angle of attack directly influenced collection efficiency along the chord of the test article. Non-zero angles created shadow regions on the suction side where the incoming cloud did not impact the test article. This can be seen in Fig. 17 where AoA varied from 0° (left), 2° (middle), and 4° (right). Increasing the AoA pushed the initial impinging area (aft of the leading edge) farther back on the suction side. These images represent 3 of the 5 tests shown earlier in Fig. 14 and tabulated in Table 2 for the AoA sweep (Block E). Figure 18 is a zoomed in view of the suction side strut junction for the AoA sweep shown in Fig. 14. These cross sections quantify the extent of icing on the main body. In addition, Fig. 18 shows the impact of AoA on the ice accretion as shadow and concentration regions can be seen on the strut. The shadow region is noticeable near the strut junction near y = 5 in. There is thicker ice accreted at the strut around y = 6 inches compared to y = 8 inches for the 4° AoA, suggesting cloud concentration caused by flow upstream around the test article leading edge.


Figure 17. Images showing extent of ice on the suction side of the test article where AoA varied from 0° (left), 2° (middle), and 4° (right). From Block E in Table 2, Test Run IDs UG3538, UG3539, and UG3540 respectively.

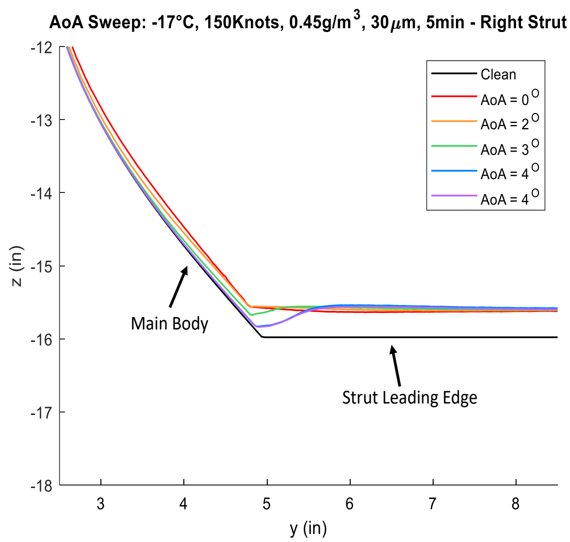

Figure 18. Cross sections at the SIDRM midspan, zoomed in on the suction side strut junction, for the AoA sweep shown in Fig. 14 (Block E).

Cloud MVD impacted ice accretion along the test article chord resulting in different icing limits downstream of the leading edge. The images in Fig. 19 show how the smaller MVD test on the left (18 μm) impinged farther downstream on the suction side as compared to the larger MVD test on the right (90 μm). These images represent 2 of the 6 tests shown earlier in Fig. 11 and tabulated in Table 2 for the MVD sweep conducted at 150 knots and 4° AoA (Block B). Figure 20 is a zoomed in view of the suction side strut junction for the same MVD sweep shown in Fig. 11. These cross sections quantify the extent of icing on the main body. In addition, Fig. 20 shows the impact of MVD on the ice accretion as shadow regions near the strut junction are more prominent for smaller MVD clouds.


Figure 19. Images showing extent of ice on the suction side of the test article where tests were conducted at 4° AoA, and MVD varied from 18 μm (left) to 90 μm (right). From Block B in Table 2, Test Run IDs UG3541 and UG3542 respectively.

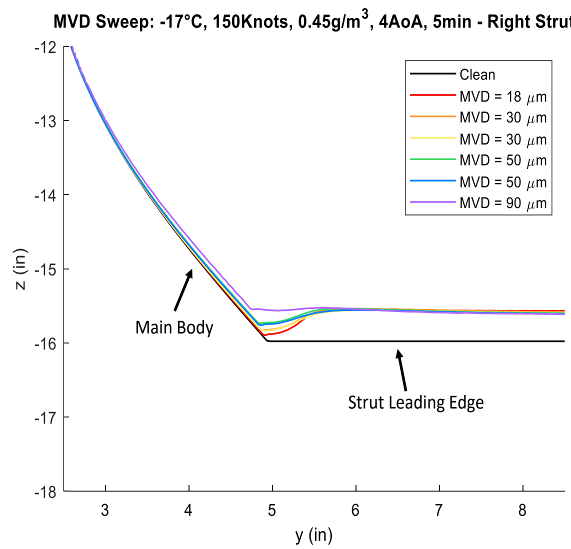

Figure 20. Cross sections at the SIDRM midspan, zoomed in on the suction side strut junction, for the MVD sweep at 150 knots and 4° AoA shown in Fig. 11 (Block B).

In the aerodynamic analysis, data suggested that flow symmetry was not at the leading edge when the test article was set to 0° AoA, but perhaps off by about 0.3°. All accretions appear symmetric and no discernable lean in accretion bias is observed in Figs. 10 and 12, the two MVD sweeps conducted at 0° AoA (Blocks A and C).

Ice Accretion Characteristics

Two primary parameters impacted icing characteristics (such as glaze/rime ice and shedding behavior): total air temperature and cloud MVD. Supercooled liquid freezes more readily upon impacting the surface with colder air temperatures, while ice accretions in warmer air temperatures result in more runback before freezing. Colder air temperature tests resulted in rime ice accretions which were characterized by opaque, white ice with more streamlined accreted geometries. The warmer air temperature tests resulted in glaze ice characterized by more transparent ice with horn shapes on leading edges. The images in Fig. 21 show the qualitative difference between a glaze ice test (T_0 = -3 °C) on the left and rime ice test (T_0 = -17 °C) on the right. These images represent 2 of the 7 tests shown earlier in Fig. 13 and tabulated in Table 2 under the total air temperature sweep (Block D).

Figure 21. Images of ice accretions from the air temperature sweep with a glaze ice accretion on the left (T_0 = -3 °C), and rime ice accretion on the right (T_0 = -17 °C). From Block D in Table 2, Test Run IDs UG3531 and UG3534 respectively.

Review of time-lapsed video showed that smaller MVD clouds resulted in greater amounts of feather shedding towards the top of the steep ramp on the test article. Images of final ice accretions from the MVD sweep at 150 knots and 0° AoA (Block A) generated from clouds of MVD = 15 µm (left) and MVD = 90 µm (right) are shown in Fig. 22. The red boxes indicate the areas where there were differences in shedding behavior. There was continuous shedding from 4 minutes into the accretion until the end of the test (10 min) for the accretion on the left. In contrast, there was virtually no shedding for the image on the right. Also, as mentioned earlier, greater amounts of shedding occurred during warmer air temperature runs compared to colder conditions. The differences in shedding can be seen in Fig. 21 in the inclined section where the strut is located.

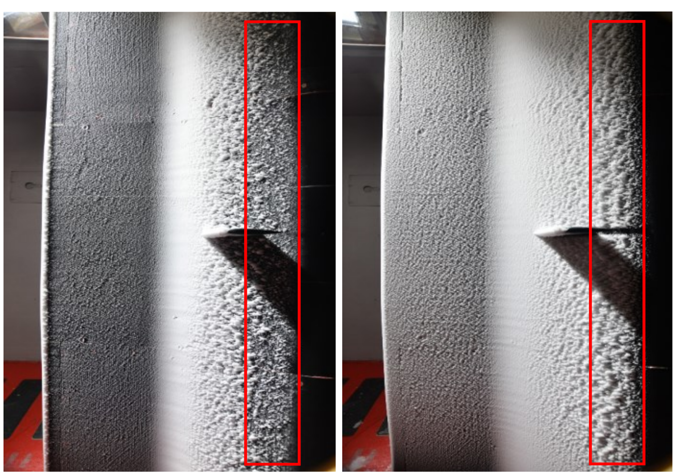

Figure 22. Images of ice accretions from the MVD sweep at 150 knots and 0° AoA where the cloud MVD equaled 15 µm on the left and 90 µm on the right. From Block A in Table 2, Test Run IDs UG3513 and UG3516 respectively. The red boxes highlight the differences in shedding behavior.

Test Article Surface Temperature

Surface temperature was measured by flush mounted thermocouples during the ice accretion process. The location of these thermocouples on the SIDRM test article are shown in Fig. 2 with nominal location provided in Table A1 of the appendix. Analysis of surface temperature data revealed that total air temperature and cloud MVD impacted surface temperature during ice accretion. A small sample of the many thermocouples is presented, which is representative and demonstrative of the overall surface temperature picture during the ice accretion process.

Figures 23 and 24 show transient temperature profiles for the total air temperature sweep (Block D) and MVD sweep (Block B) respectively. The three panels in each figure represent different midspan thermocouples measurements: A) T301 at the leading edge, B) T303 at the flat section of the test article 5 inches downstream of the leading edge, and C) T306 at the base of the curved section 12.5 inches downstream of the leading edge. The flat section refers to the linear segment of the SIDRM cross-section profile from z = -0.6 to -10.5 inches. The curved section refers to the curved segment from z = -10.5 to 16 inches of the SIDRM profile, just upstream of the strut. Icing spray time is the bottom axis, and the dashed vertical lines represent the start and end of the spray. The plots provide test article surface temperature 30 seconds prior to and after cloud activation.

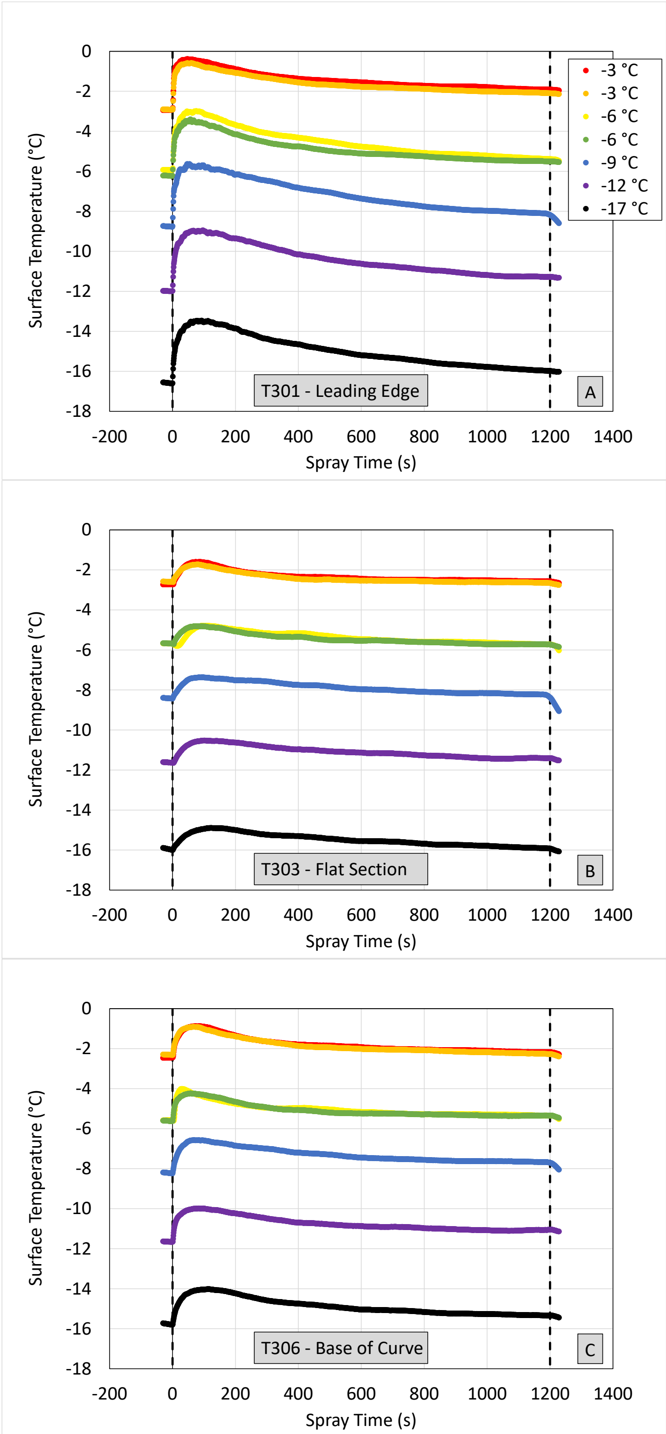

Figure 23. Transient surface temperature profiles for the total air temperature sweep (Block D) grouped by thermocouple location: A) T301 at the leading edge, B) T303 at the flat section of the test article, and C) T306 at the base of the curved section.

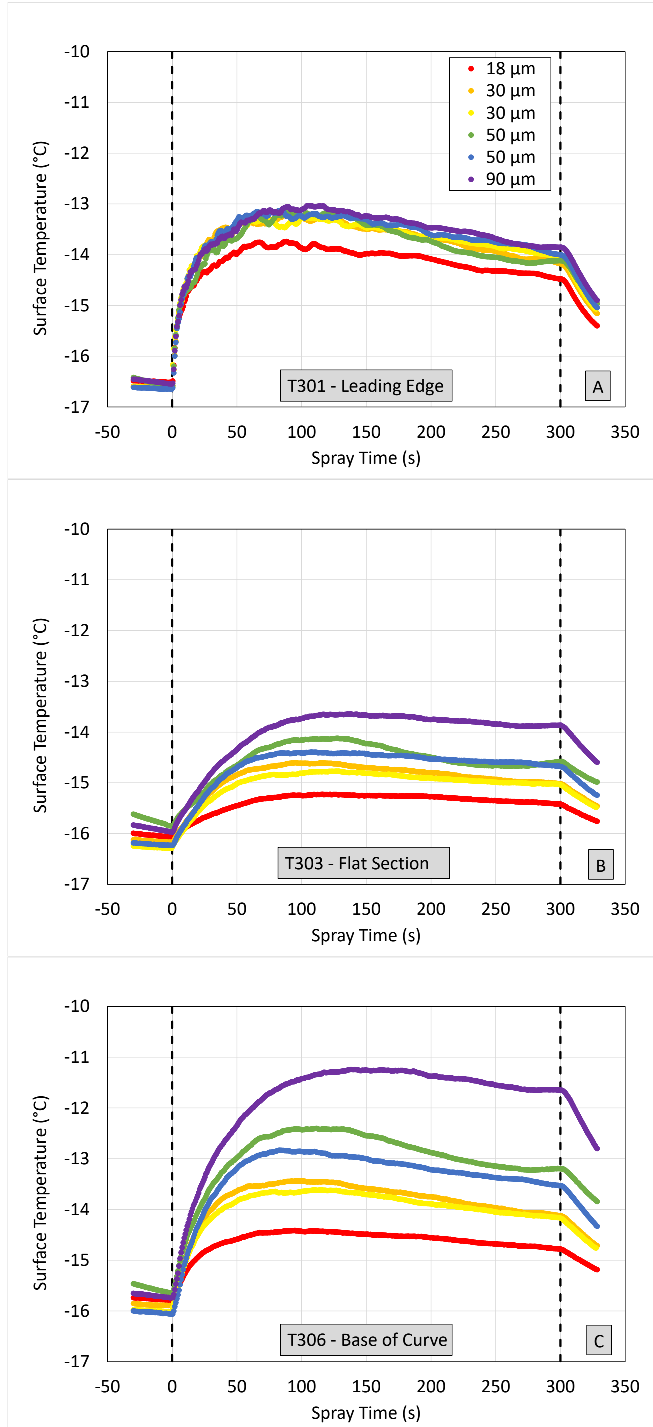

Figure 24. Transient surface temperature profiles for the MVD sweep (Block B) grouped by thermocouple location: A) T301 at the leading edge, B) T303 at the flat section of the test article, and C) T306 at the base of the curved section.

Figure 23 shows that there is an initial increase in test article surface temperature for all thermocouples as the spray cloud is activated and at every total air temperature. This increase in surface temperature is related to the release of latent heat as the supercooled liquid droplets freeze during the accretion process [17-18]. The increase in surface temperature is greater for the colder total air temperature test runs because these tests have a higher freezing fraction (rime > glaze) which release the latent heat in a shorter period of time. The supercooled droplets are approximated to be around the static wet-bulb temperature upon impact, where total air temperature is a good approximation. The increase in surface temperature is greatest at the leading edge thermocouple because the collection efficiency is greatest there, and lowest at the flat section of the test article. Greater collection efficiency is directly related to greater fusion heat release and hence greater temperature increase. The overall trend is that surface temperature deceases over time after the initial increase. Ice is a good insulator and as ice thickness increases less heat conducts towards the test article surface from the latent heat release of freezing supercooled droplets at the ice-air interface. As the spray cloud is turned off, the test article surface temperature decreases as no more heat is supplied from latent heat release of fusion. These transient temperature profiles indicate that there is good repeatability as there is good agreement between the two pairs of repeat test runs conducted at T_0 = -3 °C and T_0 = -6 °C.

The transient temperature profiles of the MVD sweep in Figure 24 (conducted at T_0 = -17 °C) are similar to profiles in the total air temperature sweep in Figure 23. All three thermocouples for all MVD test runs showed an initial increase in surface temperature followed by a slow decrease until when the spray cloud was turned off where surface temperature decreased even further. The same physics described in the previous paragraph applies for this transient trend. A larger surface temperature increase occurred for larger MVD sprays as the larger droplets were more ballistic and resulted in greater collection efficiency and by extension greater latent heat release. As in the total air temperature sweep, the smallest surface temperature rise occurred at the flat section of the test article (T303). Of note is that the largest surface temperature increase occurred at the base of the curved section (T306) during the largest MVD spray (90 µm). Collection efficiency played a role in this outcome as this sweep was conducted at 4° AoA, which slightly reduced the collection efficiency at thermocouple ID T301 and increased collection efficiency at T306 as compared to a 0° AOA run. Again, there is reasonably good agreement in measured transient surface temperature between the two pairs of repeat test runs where *MVD* = 30 and 50 µm.

Conclusion

An icing test entry was conducted with the SIDRM test article installed at the NASA IRT icing wind tunnel in early 2022. The data measured during these tests will be used to develop and validate 3D engine icing simulation tools such as GlennICE. This paper discussed measurements related to aerodynamic tests and supercooled liquid icing tests that were conducted.

Test article surface pressure was measured utilizing pressure taps that ran the length of the chord. Experimental measurements were compared to computational CFD simulations and were in good agreement for various angles of attack and airspeeds.

Various parametric sweeps were conducted during the supercooled liquid ice accretion portion of the test entry. Primary measurements included accreted ice mass, 3D scans to capture the geometry of the accreted ice, and test article surface temperature. These sweeps were performed to measure that parameter's impact on ice accretion size, location, characteristics, and test article surface temperature.

Larger cloud MVD, colder air temperatures, smaller angles of attack, and longer spray times were the primary parameters that resulted in greater ice mass. Larger droplets are more ballistic and resulted in greater collection efficiency. Colder air temperatures resulted in less shedding compared to warmer air temperature accretions (and hence less mass loss). Smaller angles of attack resulted in fewer shadow regions leading to more ice accretion. Longer spray times provide greater time to accrete more ice.

Test article angle of attack and cloud MVD impacted the location of ice accretion. Test article angle of attack directly influenced collection efficiency along the chord of the test article creating shadow regions. Cloud MVD impacted collection efficiency along the test article chord resulting in different impingement limits downstream of the leading edge as larger droplets are more ballistic and smaller droplets follow the flow.

Total air temperature and cloud MVD were the primary parameters impacting icing characteristics. Warmer air temperatures resulted in glaze ice while colder conditions resulted in rime ice accretions. Smaller MVD clouds and warmer air temperatures resulted in greater amounts of feather shedding on the steep inclined area of the test article.

Finally, total air temperature and cloud MVD impacted surface temperature during ice accretion. Surface temperature increased at the onset of accretion due to the latent heat release as supercooled liquid froze. A greater amount of instantaneous latent heat is released for supercooled droplets in colder air temperatures, resulting in a greater surface temperature increase. Larger MVD droplets are more ballistic and contribute to a high collection efficiency which in turn results in greater amounts of latent heat release and temperature increase.

References

1. Bravin, M., and Strapp, J.W., "A Continuing Investigation of Diurnal and Location Trends in an Ice Crystal Icing Engine Event Data Base," *SAE International Conference on Icing of Aircraft, Engines, and Structures*, SAE, Minneapolis, MN, 2019, SAE Technical Paper 2019-01-1964.
2. Mason, J. G., Strapp, J. W., and Chow, P., "The Ice Particle Threat to Engines in Flight," *44th AIAA Aerospace Sciences Meeting and Exhibit*, AIAA, Reno, NV, 2006, AIAA-2006-206.
3. Flegel, A. B., "Ice Crystal Icing Investigation on a Honeywell Uncertified Research Engine in an Altitude Simulation Icing Facility," *Proceedings of the ASME Turbo Expo 2020*, London, England, 2020, GT2020-14714.
4. Flegel, A. B., and Oliver, M. J., "Preliminary Results from a Heavily Instrumented Engine Ice Crystal Icing Test in a Ground Based Altitude Test Facility," *8th AIAA Atmospheric and Space Environments Conference*, 2016, AIAA-2016-3894.
5. Oliver, M. J., "Validation Ice Crystal Icing Engine Test in the Propulsion Systems Laboratory at NASA Glenn Research Center," *6th AIAA Atmospheric and Space Environments Conference*, AIAA, Atlanta, GA, 2014, AIAA-2014-2898.
6. Struk, P. M., Agui, J. H., Bartkus, T. P., Tsao, J.-C., King, M. J., and Ratvasky, T. "Ice-Crystal Icing Accretion Studies at the NASA Propulsion Systems Laboratory," *SAE 2019 International Conference on Icing of Aircraft, Engines, and Structures*, SAE, Minneapolis, MN, 2019, SAE Technical Paper, 2019-01-1921.
7. Bartkus, T. P., Tsao, J. C., and Struk, P. M. "Analysis of Experimental Ice Accretion Data and Assessment of a Thermodynamic Model During Ice Crystal Icing " *SAE International Conference on Icing of Aircraft, Engines, and Structures*, SAE Technical Paper, 2019-01-2016.
8. Struk, P. M., Ratvasky, T. P., Bencic, T., Van Zante, J. F., King, M. C., Tsao, J.-C., and Bartkus, T. P. "An Initial Study of the Fundamentals of Ice Crystal Icing Physics in the NASA Propulsion Systems Laboratory," *9th AIAA Atmospheric and*

Space Environments Conference, AIAA, Denver, CO, 2017, AIAA-2017-4242.
9. Struk, P. M., Tsao, J-C., and Bartkus, T. B., "Plans and Preliminary Results of Fundamental Studies of Ice Crystal Icing Physics in the NASA Propulsion Systems Laboratory," *8th AIAA Atmospheric and Space Environments Conference*, 2016, AIAA-2016-3738.
10. Bartkus, T. P., Lee, S., Potapczuk, M. G., and Flack. C. A., "Description of Cloud Characterization and Icing Tests for a 3D Heated Test Article at the NASA Icing Research Tunnel," *AIAA AVIATION 2022 FORUM,* AIAA, Chicago, IL, 2022, AIAA-2022-3700.
11. Bartkus, T., Potapczuk, M., Lee, S., Stewart, E., and Chen, R.-C., "Plans for Ice Crystal Icing Tests Using a 3D Heated Test Article at the NASA Icing Research Tunnel," *AIAA AVIATION 2021 FORUM,* AIAA, Virtual Event, 2021, Oral Presentation.
12. Wright, W. B., Porter, C. E., Galloway E. T., and Rigby D. L, "GlennICE 2.1 Capabilities and Results," *AIAA AVIATION 2022 FORUM,* AIAA, Chicago, IL, 2022, AIAA-2022-3309.
13. Porter, C. E., "A Comparison of Trajectory Refinement Schemes for GlennICE," *AIAA AVIATION 2022 FORUM,* AIAA, Chicago, IL, 2022, AIAA-2022-3692.
14. Wright, W., Porter, C., Galloway, E., and Rigby, D. "An Automated Refinement Process for Particle Trajectory Methods in GlennICE," *AIAA AVIATION 2021 FORUM,* AIAA, Virtual Event, 2021, AIAA-2021-2631.
15. Stewart. E. A., and Bartkus, T. P., "Computational Icing Analysis on NASA's SIDRM Geometry to Investigate Collection Efficiency," *SAE International Conference on Icing of Aircraft, Engines, and Structures*, SAE, Vienna, Austria, 2023 (submitted for consideration).
16. Brunner, C. E., Kiefer, J., Hansen, M. O., and Hultmark, M., "Study of Reynolds number effects on the aerodynamics of a moderately thick airfoil using a high-pressure wind tunnel," *Exp Fluids* 62, 178 (2021).
17. Bartkus, T. P., Struk, P. M., Tsao, J. C., and Van Zante, J. F., "Numerical Analysis of Mixed-Phase Icing Cloud Simulations in the NASA Propulsion Systems Laboratory," *8th AIAA Atmospheric and Space Environments Conference*, AIAA, Washington D.C., 2016, AIAA-2016-3739.
18. Bartkus, T. P., Struk, P. M., and Tsao, J. C., "Development of a Coupled Air and Particle Thermal Model for Engine Icing Test Facilities," *SAE International Journal of Aerospace,* Vol. 8, No. 1, 2015, pp. 15-32, SAE-2015-01-2155.
19. Hindmarsh, J., Russell, A., and Chen, X., "Experimental and numerical analysis of the temperature transition of a suspended freezing water droplet*," International Journal of Heat and Mass Transfer* 46: 1199-1213, 2003.

Contact Information

Tadas P. Bartkus, Ph.D.
Work phone: (216) 433-6915
E-mail: tadas.p.bartkus@nasa.gov
Affiliation: Ohio Aerospace Institute

Acknowledgments

The authors wish to acknowledge the financial support for this work by the Power and Propulsion sub-project of the NASA Advanced Air Transport Technology project (AATT) under NASA's, Advanced Air Vehicles Program (AAVP). In addition, the authors would also like to acknowledge the efforts made by Jordan Salkin and Quentin Schwinn in collecting and processing the 3D scanned icing geometry data that is used extensively in this technical paper.

Appendix

Tables showing the location of built-in instrumentation on the SIDRM surface are provided in the appendix.

Table A1. Table providing the nominal location of the flush mounted Type-K thermocouples.

TYPE-K THERMOCOUPLES			
TC Name	*x* (in)	*y* (in)	*z* (in)
INSTRUMENTED MAIN BODY AND STRUT			
T201	-2.500	0.000	0.000
T301	0.000	0.000	0.000
T401	2.500	0.000	0.000
T302	0.000	-0.842	-2.500
T303	0.000	-1.283	-5.000
T304	0.000	-1.723	-7.500
T305	0.000	-2.164	-10.000
T306	0.000	-2.762	-12.500
T207	-2.500	-4.196	-15.000
T307	0.000	-4.196	-15.000
T407	2.500	-4.196	-15.000
ST1	0.000	-5.34	-15.978
ST2	0.000	-5.74	-15.978
T310	0.000	-9.207	-21.480
T311	0.000	-10.546	-23.980
T312	0.000	-10.841	-26.480
T313	0.000	-10.830	-31.480
T314	0.000	-10.715	-36.480
T315	0.000	-7.716	-50.940
NON-INSTRUMENTED MAIN BODY			
BT303	0.000	1.283	-5.000
BT307	0.000	4.196	-15.000
BT311	0.000	10.546	-23.980
BT314	0.000	10.715	-36.480
BT315	0.000	7.716	-50.940

Table A2. Table providing the nominal location of the surface pressure taps.

PRESSURE TAPS			
Tap Name	*x* (in)	*y* (in)	*z* (in)
LOWER TAPS			
P101	-16.750	0.000	0.000
P102	-17.000	-0.165	-0.030
P103	-17.250	-0.289	-0.100
P104	-17.500	-0.377	-0.190
P105	-17.750	-0.437	-0.300
P106	-17.250	-0.953	-3.130
P107	-17.250	-1.505	-6.260
P108	-17.250	-2.770	-12.520
P109	-17.250	-7.127	-18.780
P110	-17.250	-9.506	-21.910
P111	-17.250	-10.777	-25.040
P112	-17.250	-10.840	-28.170
P113	-17.250	-10.831	-31.300
P114	-17.250	-10.658	-37.550
P115	-17.250	-9.907	-43.810
P116	-17.250	-8.080	-50.070
P117	-17.250	-4.794	-56.330
P118	-17.250	0.000	-62.590
P119	-17.250	0.289	-0.100
P120	-17.750	0.437	-0.300
P121	-17.250	0.953	-3.130
P122	-17.250	1.505	-6.260
P123	-17.250	2.770	-12.520
P124	-17.250	7.127	-18.780
P125	-17.250	9.506	-21.910
P126	-17.250	10.777	-25.040
P127	-17.250	10.840	-28.170
P128	-17.250	10.831	-31.300
P129	-17.250	10.658	-37.550
P130	-17.250	9.907	-43.810
P131	-17.250	8.080	-50.070
P132	-17.250	4.794	-56.330
UPPER TAPS			
P201	16.75	0.000	0.000
P202	17.000	-0.165	-0.030
P203	17.250	-0.289	-0.100
P204	17.500	-0.377	-0.190
P205	17.750	-0.437	-0.300
P206	17.250	-0.953	-3.130
P207	17.250	-1.505	-6.260
P208	17.250	-2.770	-12.520
P209	17.250	-7.127	-18.780
P210	17.250	-9.506	-21.910
P211	17.250	-10.777	-25.040
P212	17.250	-10.840	-28.170
P213	17.250	-10.831	-31.300
P214	17.250	-10.658	-37.550
P215	17.250	-9.907	-43.810
P216	17.250	-8.080	-50.070
P217	17.250	-4.794	-56.330
P218	17.250	0.000	-62.590
P219	17.250	0.289	-0.100
P220	17.750	0.437	-0.300
P221	17.250	0.953	-3.130
P222	17.250	1.505	-6.260
P223	17.250	2.770	-12.520
P224	17.250	7.127	-18.780
P225	17.250	9.506	-21.910
P226	17.250	10.777	-25.040
P227	17.250	10.840	-28.170
P228	17.250	10.831	-31.300
P229	17.250	10.658	-37.550
P230	17.250	9.907	-43.810
P231	17.250	8.080	-50.070
P232	17.250	4.794	-56.330